Welding in the World
https://doi.org/10.1007/s40194-025-02010-9

RESEARCH PAPER

On the role of rotational speed in P-FSSW dissimilar aluminum alloys lap weld

Mariia Rashkovets[1,2] · Giuseppe Dell'Avvocato[3] · Nicola Contuzzi[1] · Davide Palumbo[1] · Umberto Galietti[1] · Giuseppe Casalino[1]

Received: 30 September 2024 / Accepted: 5 March 2025

Abstract

One of the most promising solid-state methods for joining high-strength aluminum alloys, friction stir spot welding (FSSW), remains hindering due to formation of the keyhole defect. This paper presents its promising variation as a probeless-friction stir spot welding (P-FSSW) assisted by flat featureless shoulder. Based on the prior arguments on the feasibility of this method in joining aluminum alloys, present work provides in-depth study on the effect of rotational speed on microstructure, phase transformations, and final properties of dissimilar aluminum plates, studies using scanning electron microscopy (SEM), occupied by electron backscattered diffraction (EBSD) method and energy-dispersive X-ray spectroscopy (EDS) analysis. The resulting properties was examined through microhardness measurements and tensile-shear testing. Results showed that rotational speed plays a crucial role in determining the intensity of material softening, its flow, and mechanical properties. Uniform heating and circumferential material flow helped eliminate edge hook defects using a featureless tool during P-FSSW. The microstructure development followed progressive plastic deformation was accompanied by a gradual transition between continuous dynamic recrystallization (CDRX) and dynamic recovery (DRV) process. The re-precipitation of the Al_2CuMg phase restricted grain growth by pinning recrystallized grains within the stir zone (SZ). Mechanical tests indicated improved joint strength, suggesting that P-FSSW could produce high-quality, lightweight joints suitable for automotive and aerospace applications.

Keywords Probeless friction stir spot welding · Microstructure · Dynamic recrystallization · Mechanical test

1 Introduction

Weight reduction is a paramount concern across various industries. Lightweight structure, primarily joined using spot welding, serves this issue. While, the replacement of traditional ferrous alloys with high-strength-to-weight ratio materials like aluminum alloys offers great weight reduction, joining of the final assemblies through fusion welding methods, such as resistance spot welding (RSW), presents several challenges [1]. Friction stir spot welding (FSSW), a variant of friction stir welding (FSW) for single-point joining, has gained significant attention as a solid-state alternative to the widely used RSW [2]. The principle of FSSW based on simultaneously heating and stirring the plasticized material using a non-consumable rotating tool, thereby effectively suppresses liquid-phase defects [3] and offers cost-effectiveness [4, 5]. Nevertheless, several drawbacks still hinder its widespread industrial application. One of the most significant limitations is the formation of a centerline keyhole defect caused by the tool's probe (pin) [6].

Several modifications of FSSW have been proposed to overcome keyhole formation, including swept pattern [7], two-step FSSW with circular pattern [8], double-side FSSW [9], flat FSSW [10], friction spot extrusion [11], and refill FSSW (RFSSW) [12]. However, most listed processes

Recommended for publication by Commission III - Resistance Welding Solid State Welding And Allied Joining Process.

✉ Nicola Contuzzi
nicola.contuzzi@poliba.it

[1] Department of Mechanics, Mathematics and Management, Polytechnic University of Bari, 70125 Bari, Italy

[2] World-Class Research Center «Advanced Digital Technologies», State Marine Technical University, 190121 St. Petersburg, Russia

[3] Department of Industrial and Information Engineering and Economics, University of L'Aquila, 67100 L'Aquila, Italy

involve intricate material flow that preserves other defects like edge hook that significantly affects the final mechanical properties of spot welds. The crack initiates at the hook tip as the highest stress concentration point [13]. Other studies have also indicated that both residual stresses and the inhomogeneous microstructure resulting from the abrupt transition boundary region can significantly contribute to failure of friction-based welds [14]. For instance, Tra et al. [15] studied fatigue crack growth and concluded that the crack growth rate is less influenced by residual stresses and more by the inhomogeneous microstructure. Many studies have been conducted to ensure defect-free joints with a smooth microstructure transition in friction-based welds, providing various assisted approaches, among them utilization of ultrasonic vibration [16], mechanical vibrations [17], or laser-assisted techniques [18]. However, such methods often require complex equipment or keep the keyhole defect.

In 2010, Bakavos et al. [19] and Tozaki et al. [20] pioneered the simple elimination of the keyhole, using a probeless (pinless) tool. Probeless friction stir spot welding (P-FSSW) aims a similar approach as classic FSSW with the tool consisting solely of the shoulder, which can be either featured or featureless. As a result, the probeless tool promoted a significant increment in final mechanical strength due to a larger effective bonding area. To date, numerous studies have reported successful outcomes using P-FSSW with different featured shoulders on high-strength aluminum alloys [20–28] and their dissimilar combinations [29–35]. However, the formation of extensive material flow regarding the design of shoulder feature still may contribute to the edge hook defect, forming two distinct fracture modes: shear and plug [13, 36, 37]. Studies of Chu et al. [38] and Li et al. [21] concluded about inability to eliminate edge hooking in P-FSSW assisted by featured shoulders, no matter how to regulate process parameters, confirming that its formation is primarily influenced by the design of shoulder features. However, recently, Contuzzi et al. [27] proposed a compromise to overcome edge hook formation by utilizing a flat featureless shoulder. However, the final mechanical properties were not evaluated.

Beyond defect formation, the material undergoes significant microstructural alterations during intense plastic deformation at elevated temperatures. The grain structure experiences varying thermal histories and transformations within the different zones of friction-based welds [39]. The stir zone (SZ) is affected by the highest temperature and strain, resulting in a fine grain structure, which generally positively influences mechanical properties following the Hall–Petch relationship. This behavior is particularly promising for P-FSSW applications as a surface mechanical treatment [40]. However, the grain structure of high-strength aluminum alloys does not completely determine final mechanical properties.

Strengthening mechanism of high-strength aluminum alloys combine both solid solution and precipitation hardening. The latter involves the formation of multiple metastable phases, such as Guinier–Preston zone (GP), semi-coherent Guinier–Preston-Bagaryatsky (GPB) zones (S"), semi-coherent Al2CuMg (S'), and incoherent stable Al2CuMg (S) [41]. This multiple phase composition continuously evolves mechanical properties. For instance, the coarsening of S'(S)-phases within the thermo-mechanically affected zone (TMAZ) and heat affected zone (HAZ) tend to reduce the microhardness within the classic FSSW welds [42]. Consequently, it is necessary to consider a balance between grain structure and precipitation phases.

The findings on the promising solid-state method of P-FSSW show that prior studies [21, 25–28] have mostly focused on material flow, rather than complex understanding of full microstructure development including both grain structure and phase composition, as well as their relationship with final mechanical properties, especially for flat featureless shoulder. Thus, the present study addresses in-depth analysis of P-FSSW using a flat featureless tool to understand the structural response of dissimilar thin plates of Al-Cu-Mg (AA2024-T3) and Al–Mg-Si (AA6082-T6) aluminum alloys. In particular, based on our previous results, the influence of rotational speed as one of the main process parameters on weld seam formation will be discussed. Optical and scanning electron microscopy, occupied by EBSD and EDS analysis, were employed to investigate the mechanisms behind the microstructure development and phase transformation under the flat featureless shoulder. The effectiveness of P-FSSW in joining aluminum plates was evaluated through tensile testing.

2 Materials and methods

Lap joints were done with overlapped plates of 2024-T3 aluminum alloys (thickness 1.5 mm) and 6082-T6 (thickness 0.8 mm) using P-FSSW with flat featureless shoulders. The standard chemical compositions of materials are presented in Table 1 [43, 44]. The average grain sizes of AA-2024-T3 and AA6082-T6 aluminum alloys were measured using the planimetric method to be ~ 12.3 µm and ~ 6 µm, respectively. The schematic representation of the experimental configuration and dwell stage of the P-FSSW process are shown in Fig. 1. The process parameters are listed in Table 2. The range was chosen based on our prior study [27].

Tensile lap shear tests were performed using an MTS Model 370 Load Frame with a load cell capacity of ± 100 kN at a 1 mm/min rate. To guarantee axial loading on the specimens during testing, the end sections of both welded plates were removed and used as spacers between the plates and the grips. This ensured symmetrical loading and eliminated

Table 1 Chemical composition of materials

Alloy	Element content, wt.%								
	Al	Cu	Mg	Mn	Si	Fe	Cr	Zn	Ti
AA2024	Bal	3.8–4.9	1.2–1.8	0.3–1.0	≤0.5	≤0.5	≤0.1	≤0.2	≤0.15
AA6082	Bal	≤0.1	0.6–1.2	0.4–1.0	0.7–1.3	≤0.5	≤0.25	≤0.2	≤0.15

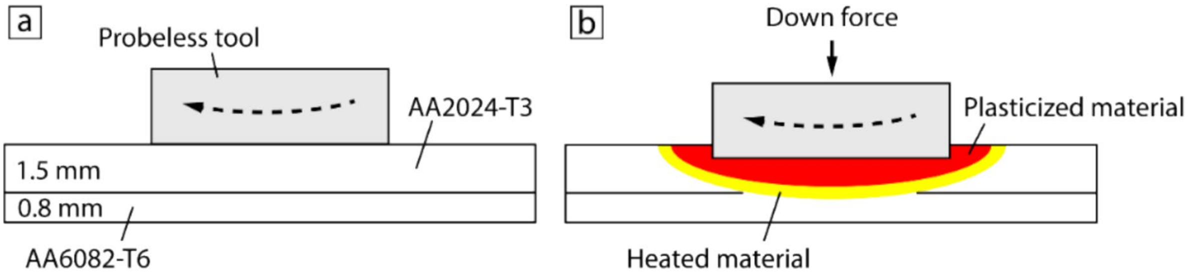

Fig. 1 Schemes of (**a**) the workpiece and (**b**) the dwelling stage of P-FSSW

Table 2 Process parameters of P-FSSW

Test	Rotational speed, rpm	Downforce, N	Dwell time, s
S-1	2500	4900	90
S-2	2000		
S-3	1500		
S-4	1000		
S-5	500		

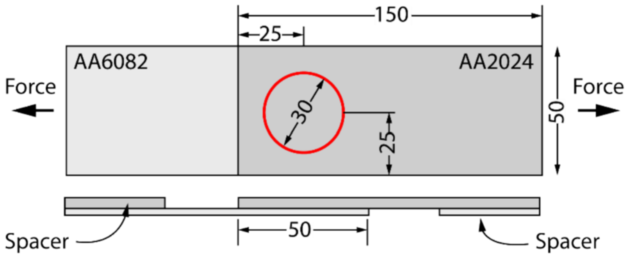

Fig. 2 Scheme of tensile test

potential bending. The scheme of the overlapped specimen is presented in Fig. 2. Triplicate tests were carried out for each welding parameter. The maximum force was considered an indicator of mechanical strength due to the inability to identify the correct state of stress in spot weld joints [45, 46].

The samples were cut using a metallographic cut-off machine. The final microstructure of cross-sectional joints was studied using an optical microscope after surface etching with Keller's reagent: 2.5-ml HNO_3, 1.5-ml HCl, 1-ml HF, and 95-ml distilled water. EBSD analysis was performed along the transverse direction (TD), i.e., the normal direction (ND) was vertical, and the rolling direction (RD) was horizontal. Samples were electropolished with a solution of 10% $HClO_4$ and 90% C_2H_6O under a potential of 20 V for 50 s. Vickers microhardness test was done on the cross-section of P-FSSW welds under 980 mN load and 3 s of dwell time.

3 Results and discussion

3.1 Weld surface

Figure 3 depicts the upper view of the spot welds for all samples. Higher rotational speed promoted an increased actual contact area between the tool and workpiece surface in samples S-3, S-2, and S-1 with the formation of smooth wear along the entire contact area. In contrast, lower rotational speed promoted the formation of numerous shallow grooves within a smooth wear of welding radius in samples S-5 and S-4. Apparently, this behavior experienced transient slip-stick contact conditions between the shoulder and workpiece surface discussed by Reilly et al. [47], resulted in failed spot welds. Thereby, these samples were excluded from further discussion.

3.2 Microstructure and material flow

3.2.1 Overall microstructure

The overall cross-sectional view of the spot welds indicated gradual and uniform heating during P-FSSW without cracking (Fig. 4). The interfaces underwent axisymmetric plastic deformation beneath the entire shoulder diameter. It is worth noting that the overall shape of the deformed region differed

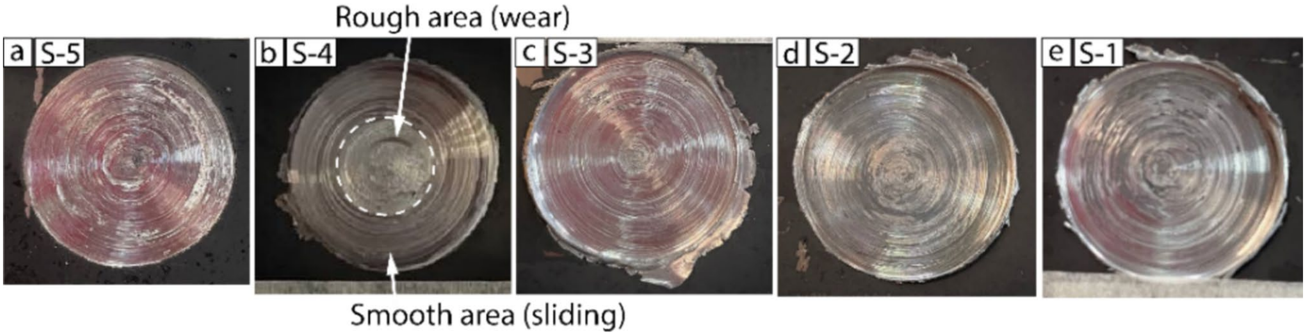

Fig. 3 Spot welded surface of samples: S-5 (**a**), S-4 (**b**), S-3 (**c**), S-2 (**d**), and S-1 (**e**)

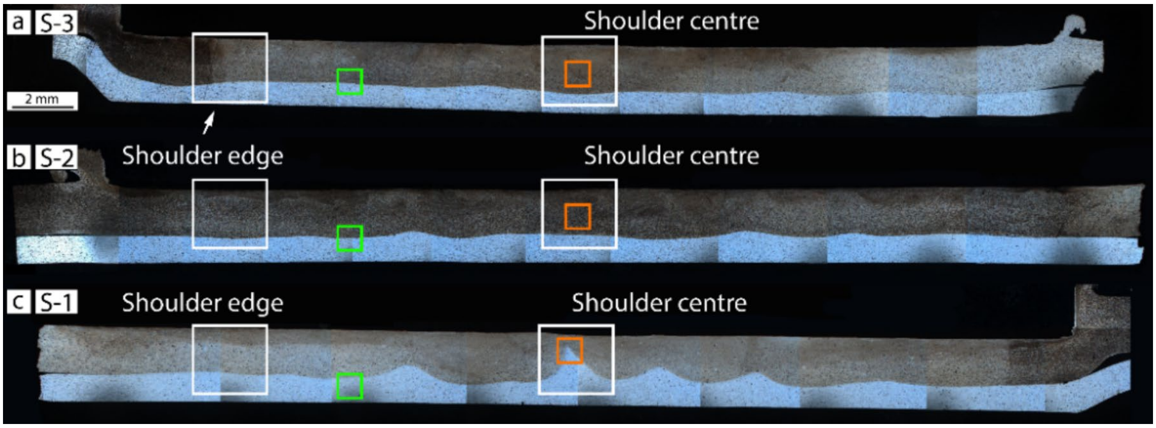

Fig. 4 Cross section of the spot welds: sample S-1 (**a**), sample S-2 (**b**), and sample S-3 (**c**). Green boxes indicate the regions of EBSD analysis; white boxes represent the area of optical and SEM examination

from the classic basin-like shape after P-FSSW with the flat featured shoulder [e.g., 28].

The intensive discrepancy of the material flow velocity between two plates during lap joint processing facilitated the breaking of continuous surface oxide films, exposing clean surfaces for metallurgical bonding [48]. Consequently, the pronounced waving of mechanical interlocked interfaces was formed in sample S-2 (Fig. 4b). The mitigation of the downward material flow through the weld center due to absence of shoulder features eliminated the upward bending of the interface between two plates. Thus, samples did not contain edge hook defects typical for P-FSSW with flat featured shoulders [36, 38]. However, sample S-2 experienced the evolution of a centerline hook due to circumferential material flow induced by the increased rotational speed and associated material softening (Fig. 4c).

The macrostructure of the spot welds represented typical zones after P-FSSW (Fig. 5b–e). These zones have been defined from the surface toward the bulk of the workpiece as follows: the stir zone (SZ), the thermo-mechanically affected zone (TMAZ), the heat-affected zone (HAZ), and the base metal (BM). The SZ alongside the surface region contained refined grains after dynamic recrystallization (further referred to as DRX), a characteristic microstructure of aluminum alloys subjected to severe plastic deformation at high temperatures [39]. Thus, the variation in SZ thickness observed in the upper plate may provide a clear indication of the extent of material plasticization between spot welds produced at different rotational speeds.

Indeed, a near-linear relationship was observed between SZ thickness and rotational speed (Fig. 5a). However, the rotational speed of 2500 rpm significantly increased material flow along the joining interface resulted in a wider confidence interval (Fig. 5d–e). In contrast, spot welds joined at 1500 rpm (sample S-1) and 2000 rpm (sample S-2) displayed a slight difference in the deformation of their joining interface (see Fig. 5b–c). Despite this, the SZ depth ratio in sample S-2 was notably higher, approximately 1.3 times that of sample S-1. This behavior suggested a more uniform temperature distribution within the material during processing at 2000 rpm.

The difference between plastic deformation along the joining interfaces depended on the TMAZ, which underwent both thermal effects and mechanical distortion induced

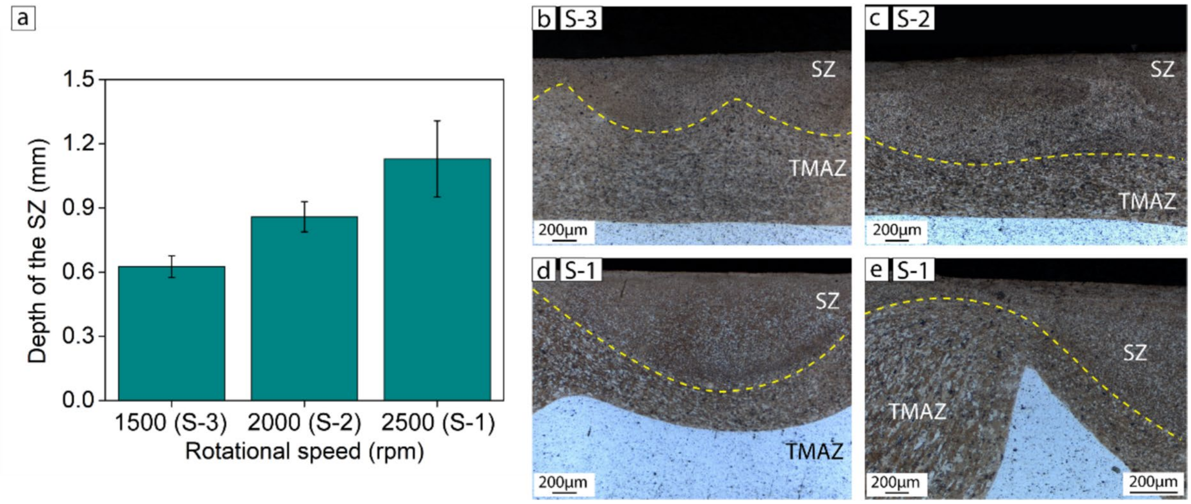

Fig. 5 (**a**) Depth of the SZ along the total thickness of the upper plate across all samples. Optical microscopy along the interface between plates in samples: (**b**) S-3, (**c**) S-2, and (**d**–**e**) S-1

by the stress within the SZ. When the SZ depth exceeded half the thickness of the upper plate, samples S-2 and S-1 experienced penetration of the TMAZ into the lower plate (Fig. 5c–e). In contrast, sample S-3 mainly retained the TMAZ within the upper plate (Fig. 5b). Consequently, sample S-1 and S-2 underwent complete mechanical interlocking and metallurgical bonding, while sample S-3 likely experienced diffusion bonding within the HAZ at elevated processing temperature.

3.2.2 Microstructure within the transition area between SZ and TMAZ

The microstructure within the transition area from the SZ to TMAZ was highly dependent on the variation of rotational speed. Sample S-3 made at the lowest value of 1500 rpm experienced a sharp SZ-TMAZ microstructure transition (Fig. 6a–b). The inverse pole figure (IPF) maps showed that grains of TMAZ contained numerous low-angle grain boundaries (LAB, green lines with a misorientation angle of 2…15° on Fig. 7a, d). A large amount of LAB indicated the presence of subgrains facilitated by dynamic recovery (further referred to as DRV) during thermo-mechanical loading of sample S-3. Further increase in amount of high-angle grain boundaries within the SZ (HAB, red lines with a misorientation of angle > 15° on Fig. 7a, d) corresponded to the progressive transformation of subgrains into the fine equiaxed structure via the DRX process [48].

The distinguishing feature of samples made at elevated rotational speed of 2000 rpm and 2500 rpm was the formation of an ultrafine grain structure along the subsurface layer of the SZ (Fig. 6c–f). Several studies have mentioned a similar region forming after the initial penetration of the rotational probe into the upper plate during classic FSSW [49–51]. These areas experienced intense shear stress and localized flow at high strain rates, thereby promoting a rapid transformation of grains into an ultrafine or even nanostructured state. Similar behavior might be found in a tribo-layer under sliding wear when shear bands develop parallel to the worn surface [52]. Consequently, the presence of the subsurface layer with an ultrafine structure indicated a transition to a regime of intense shear stress in samples S-2 and S-3.

An increased shear stress gradually amplified material softening from the center area beneath the shoulder. Thus, sample S-2 exhibited two distinct SZ-TMAZ transition boundary regions. A sharp boundary was observed near the shoulder edge (Fig. 6c), while a gradual transition with mixed grain structure occurred at the centerline (Fig. 6d). Increasing the rotational speed to 2500 rpm further intensified material softening and expanded the gradual transition throughout the entire area in sample S-1 (Fig. 6e–f). The nature of the gradual transition regions was composed of an alternating layered structure with grains of varying sizes in a manner of classical onion ring microstructure in friction-based welds [53]. However, the formation of the onion ring structure in classic FSW is explained by the detachment of the shear layers at the trailing edge of the tool during each revolution along the weld line between the workpieces [54]. In contrast, the nature of the mixed areas in P-FSSW is the result of differences within the material itself.

EBSD analysis identified progressive grains alignement towards [101] direction in the SZ of sample S-2 (Fig. 7b, e) that is suggestive of large strains being active within this reagion [55]. Simultaniously, this structure contained strings of ultrafine grains (Fig. 7j). Consequently, during continuous themo-mechanical processeing ultrafine grains

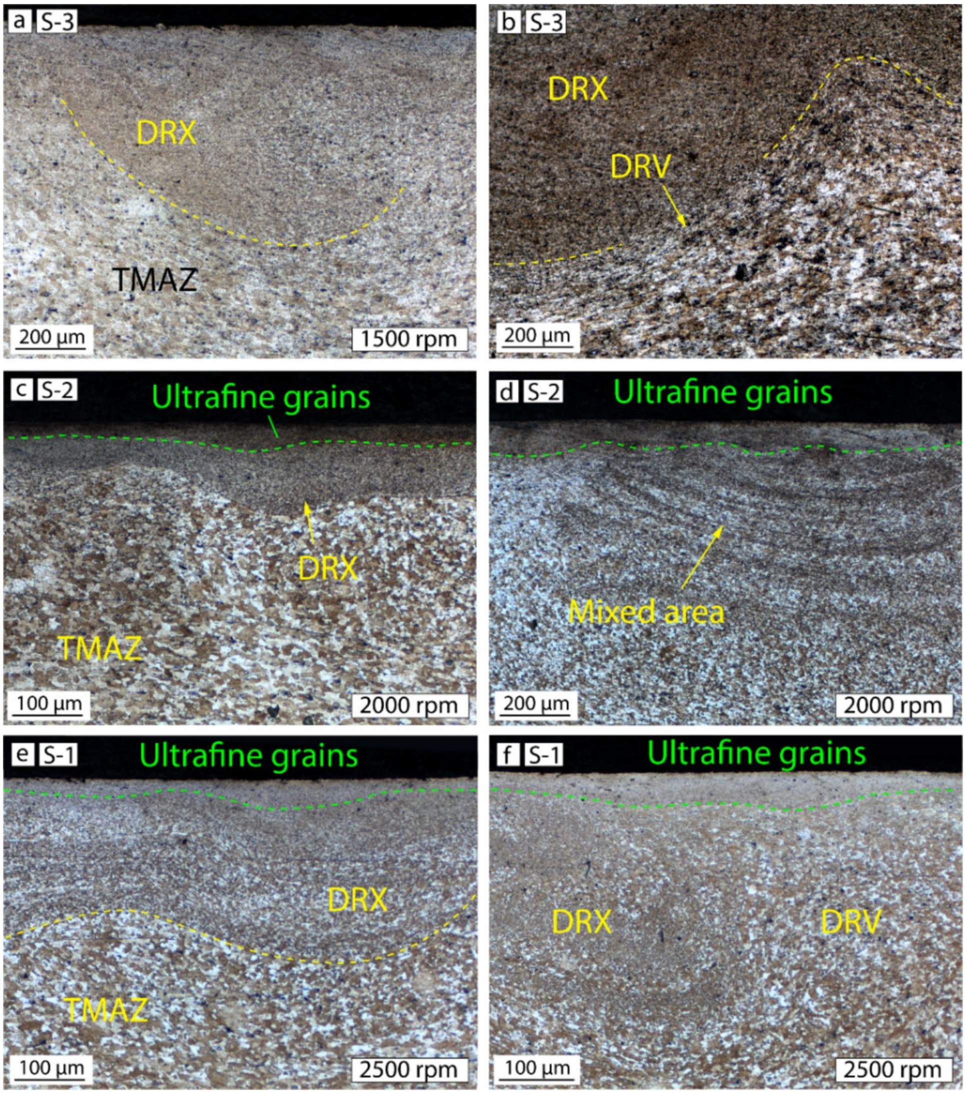

Fig. 6 Microstructure within the upper plate at the shoulder center area (**b**, **d**, **f**) and the shoulder edge region (**a**, **c**, **e**) in samples: S-3 (**a**–**b**), S-2 (**c**–**d**), and S-3(**e**–**f**). The analyzed areas are mentioned with white boxes in Fig. 4

from the subsurface layer have been embedded within the DRX structure of the SZ as continuous bands due to intense local stirring and mechanical mixing. Similar behavior was occurred within the SZ-TMAZ transition area while intermixing between DRX grains of the SZ and DRV structure of the TMAZ reagion (see Fig. 6d). Therefore, the microsctruture with the SZ transition boundary of SZ-TMAZ has expetienced layered behavior of differet charachteristic. In contrast, the main microstructure development within the TMAZ underwent a gradual transformation. As shown in Fig. 7i, the deformed grains within the TMAZ experienced a typical transverse subdivision into the near-equiaxed grains delineated by LABs [56]. Consequently, these LABs have continuously absorbed dislocations through DRV processes until a higher temperature and larger strain rates promoted progressive increase over a critical misorientation angle, eventually transforming LABs into HABs, and thus producing a recrystallized structure (Fig. 7i–j).

Of particular interest was the heavily plasticized centerline part of sample S-3 (see Fig. 4c). This region contained a comparative amount of LAB and HAB, suggesting continuous deformation (Fig. 7f) [57] despite the prominent [101] grain orientation withinh the centroline hook (Fig. 7c). Furthermore, the surrounding regions of the hook displayed distinct grain structures, evident in the optical microscopy images (see Fig. 5e). Such uneven behavior may be compared to the microstructure on the advanced (AS) and retreating sides (RS) after classic FSW [58]. Consequently, grains on the left side were significantly elongated in the direction of the intensive circumferential material flow, thereby essentially thinned due to the geometrical effect of the strain. The formation of LAB within the interiors of such deformed grains conclusively suggested DRV process (Fig. 7h). In contrast, the microstructure of the hook's interior and the right side revealed

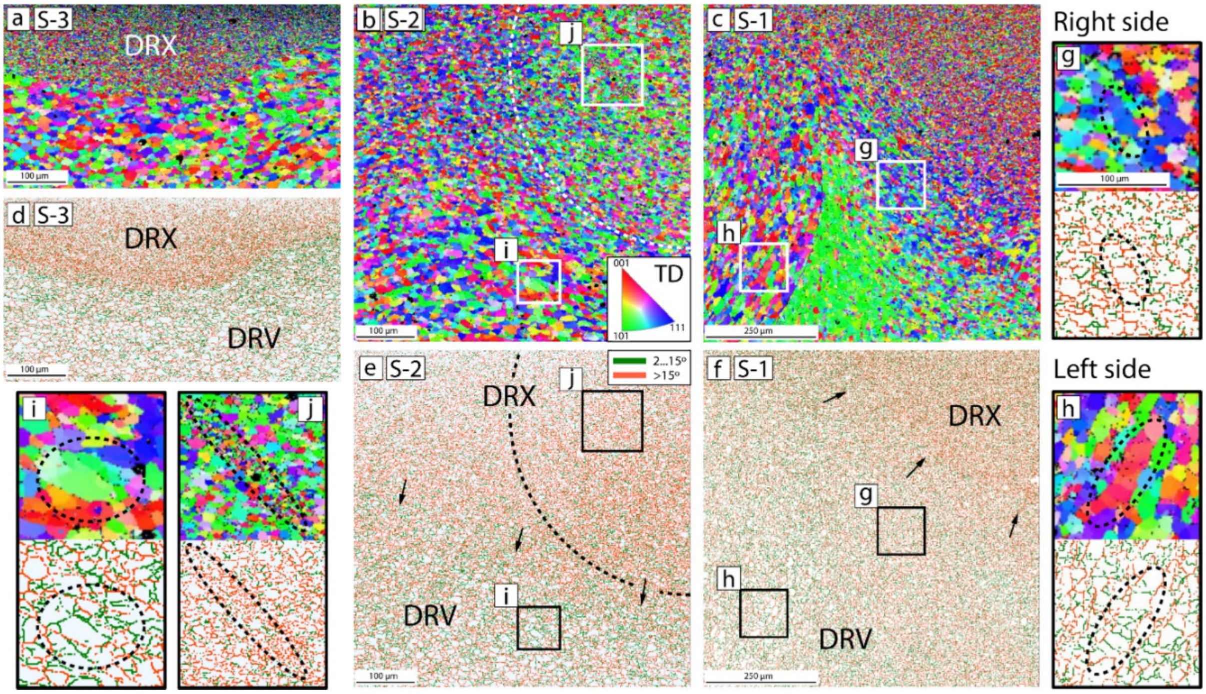

Fig. 7 EBSD IPF maps and the corresponding distribution of grain boundary misorientation angle in samples S-1 (**a**, **d**), S-2 (**d**, **e**), and S-1(**c**, **f**). The analyzed areas are mentioned with orange boxes in Fig. 4. In particular, this figure reflected: grain structure of the SZ (**j**) and TMAZ (**i**) in sample S-2; grain structure in sample S-1 around the hook on the left (**g**) and the right (**h**) side. LABs and HABs are depicted as green and red lines, respectively. Arrows indicate the transition between DRV and DRX regions

DRX grain of similar shapes and sizes as the subgrains formed by subdivision on the left side (Fig. 7g).

The mechanism of the LAB-into-HAB transition under high-strain conditions remains under a dispute. Aluminum-based alloys rather undergo two potential mechanisms for DRX: geometric DRX (GDRX) and continuous DRX (CDRX), both of which owing to a high stacking fault energy (SFE) [39]. On the one hand, the pronounced grain structure alignment along the [101] plane within the hook region suggests a low orientation difference between neighboring grains, potentially indicating GDRX as a deform mechanism [59, 60]. On the other hand, the formation of characteristic serrations at HABs of lamellar grains [39] was not observed in the present study. Thus, the observed microstructure did not fully comply with the features of GDRX. Furthermore, comparing these regions to the advancing side (AS) and retreating side (RS) of classic FSW suggests that the right side and the the hook's interior experienced higher strain rates than the left side [58]. Therefore, the dominant mechanism of microctructure development could be classified as CDRX. The fine equiaxed grain structure, coupled with a high fraction of high-angle grain boundaries (HABs), facilitated grain boundary sliding within the hook region. Concurrently, progressive grain rotation occurred within the right side of the hook. Notably, despite the extensive deformation within the SZ, a portion of low-angle boundaries (LABs) persisted within the grain interiors.

3.2.3 Microstructure along the joining interface

To study the influence of the rotational speed on the microstructure development along the joining interface, the regions close to the shoulder edge were analyzed for each sample (see Fig. 4, green boxes). The dominant deformation mode during P-FSSW is expected to be simple shear with the tangential direction to the tool surface, similar to classic FSSW processes [57, 61]. This is supported by Fig. 8, which demonstrates an increase in grain boundary rotation with increasing rotational speed, indicative of the growing influence of shear and pressure forces acting towards the lap interface. Thus, the inverse pole figure (IPF) plots showed a progressive alignment of the grain structure along the joining interface towards < 001 > of TD from sample S3 to S1 (Fig. 8e). Simultaneous gradual increase in LAB stated an increment in grain subdivision by DRV, as stated earlier. It is seen that the subgrains experienced a small deviation in the crystallographic direction from the initial state (marked by the dotted oval in Fig. 8), which suggests grain rotation and extensive grain-boundary evolution [62]. Consequently, compared to sample S-3, sample S-1 exhibited a finer grain structure, indicating higher strain levels experienced by

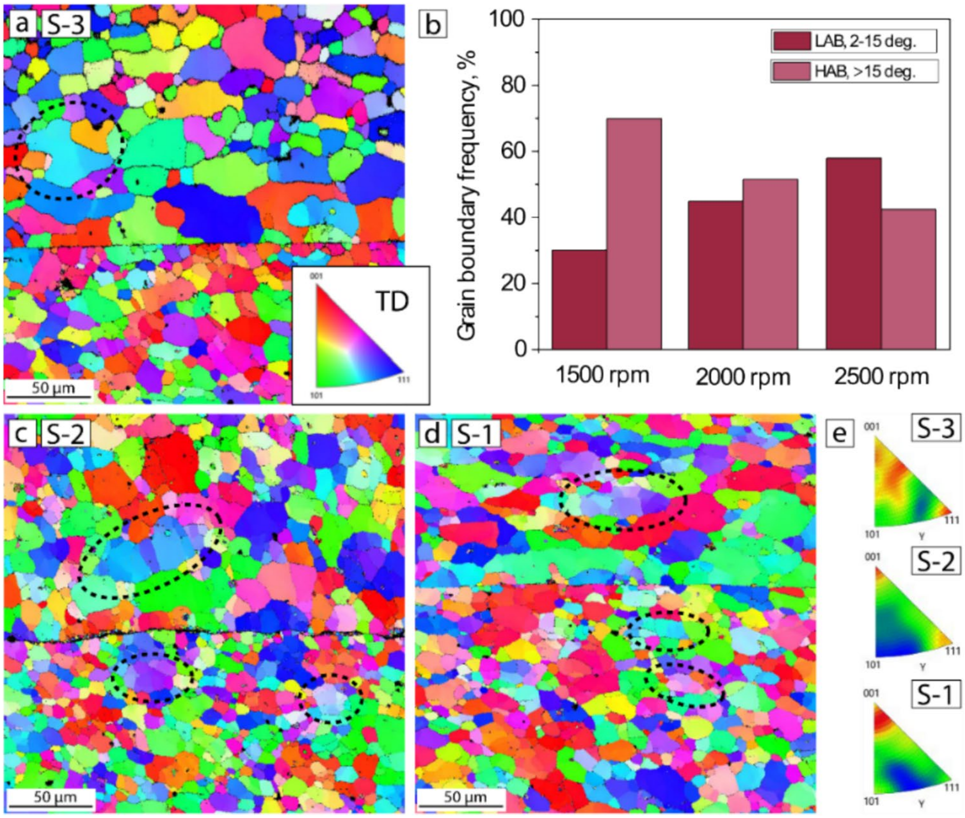

Fig. 8 EBSD IPF maps and corresponding IPF plots (**e**) along the joining interface in samples: S-3 (**a**), S-2 (**c**), and S-1 (**d**). Fractions of HAB and LAB grain boundaries along the joining interface (**b**). The analyzed areas are mentioned with green boxes in Fig. 4

the material towards the second plate and the formation of mechanical interlocking and metallurgical bonding.

3.3 Phase distribution

The BSE SEM images of SZ and TMAZ within the upper plate are shown in Fig. 9. The CDRX-induced structure has enhanced the intense re-precipitation of fine Al_2CuMg S''(S')-phases within the homogeneous distribution of Mg in a solid-solution matrix along the SZ (Fig. 9a–c). Conversely, these phases retarded the grain growth during the welding cycle through Zener pinning, resulting in an equiaxed fine-grained microstructure within the SZ. The rare appearance of large AlFeMnSi intermetallic precipitates was also observed within the SZ (Fig. 9b). These precipitates likely originated from insoluble phases primarily arise from Fe and/or Si segregation [63].

In contrast, complex AlCuMgFeMnSi intermetallic particles of variable chemical composition and irregular shapes within the TMAZ experienced a notable increase in size with higher rotational speed (Fig. 10). The results of point spectra indicated the uneven elemental distribution within the coexisting clusters of these intermetallic phases (Fig. 10d and e, Table 3). Such elemental deviation might indicate the presence of coexisting precipitates of Al_2Cu and AlCuFeMnSi [64]. Moreover, separate large Al_2CuMg S'-phases were also fixed within the TMAZ (Fig. 9d). Therefore, being temperature-dependent, the complex particles changed in size and composition due to solid-state diffusion facilitated by severe thermomechanical conditions under a higher rotational speed. Namely, an increase in deformation-induced dislocation density accelerated diffusion processes and would enhance the precursors for further precipitation phases [63].

The lower aluminum plate has also experienced slight changes in phase composition with increasing thermal load during P-FSSW such as an increment in size and volume fraction of complex intermetallic particles (bright phase) alongside the stable Mg_2Si precipitates (dark phases), as indicated in Fig. 10.

3.4 Microhardness

The microhardness distribution across the joining interface of each sample is shown in Fig. 11. The microhardness of the lower plate remained equivalent to its initial value due to keeping the strengthening by Mg_2Si precipitates within the aluminum matrix. In contrast, the microhardness within the upper plate experienced some variations such as a slight decrease along the surface region. Such behavior was attributed to the extensive microstructural refinements owing to CDRX. The re-precipitation

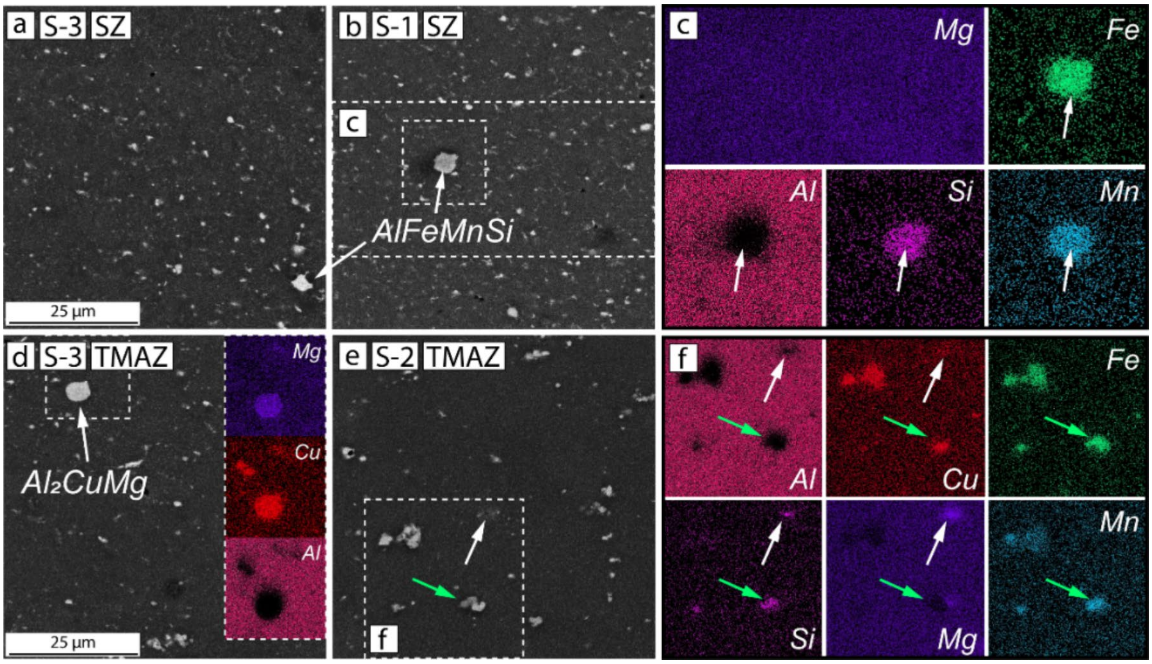

Fig. 9 BSE SEM of the SZ and TMAZ within the upper plate in samples (**a**, **d**) S-3, (**b**) S-1, and (**e**) S-2. Element mapping of marked areas within the TMAZ in samples (**c**) S-1 and (**f**) S-2

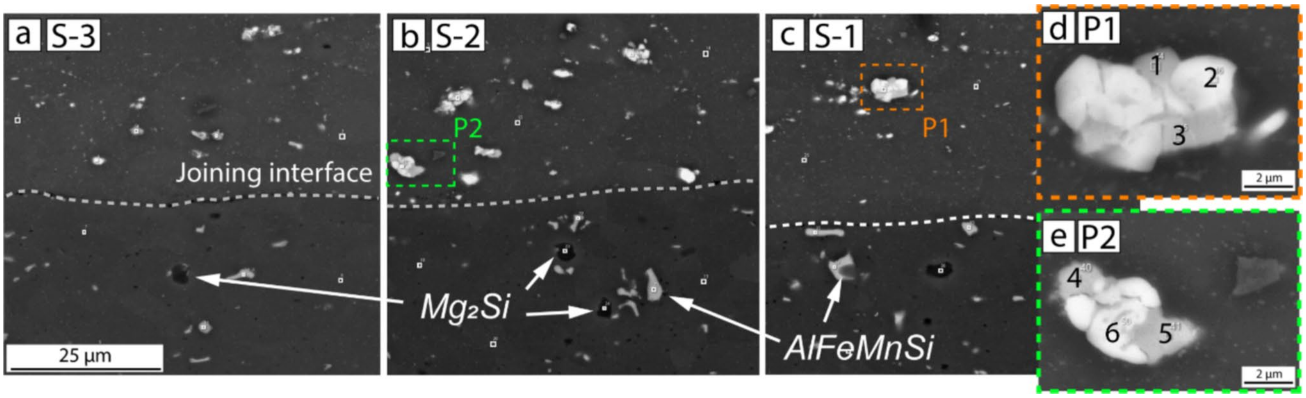

Fig. 10 BSE SEM of the joining interface in samples (**a**) S-3, (**b**) S-2, and (**c**) S-1. (**d–e**) Magnified images of complex intermetallic phases within the upper plate

Table 3 EDS results of point spectra from Fig. 10d (particle 1) and Fig. 10e (particle 2), wt.%

	Element content, wt.%					
	Al	Cu	Mg	Mn	Si	Fe
Particle 1						
Point spectra 1	69.02	15.24	0.45	12.24	0.52	2.55
Point spectra 2	63.62	24.11	0.41	7.76	0.66	7.76
Point spectra 3	66.35	10.96	0.47	11.97	3.51	11.97
Particle 2						
Point spectra 4	63.62	24.11	0.41	3.44	0.66	7.76
Point spectra 5	86.56	5.96	0.74	2.67	0.97	3.09
Point spectra 6	95.12	3.46	0.99	0.43	-	-

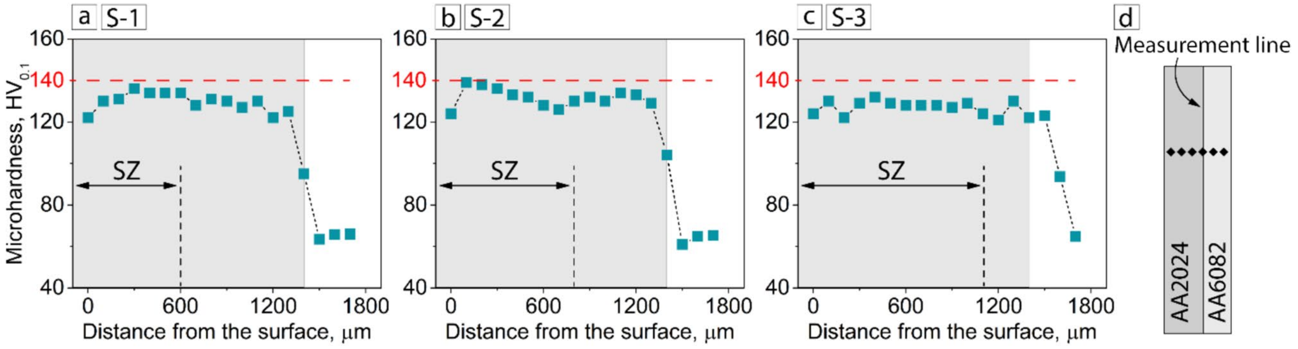

Fig. 11 Microhardness distribution across the joining line in samples: (**a**) S-1, (**b**) S-2, and (**c**) S-3. (**d**) Scheme of microhardness measurement

of Al_2CuMg phases had less impact on the strengthening mechanism [64]. Thus, despite the significant grain refinement, the material experienced a slight softening within this region. Nevertheless, the subsequent area of the SZ, characterized by a less refined grain structure and larger Al_2CuMg particles, showed a stable distribution with a slight increase in microhardness. This behavior was also attributed to the solid-solution hardening effect induced by the presence of Mg atoms inside the matrix (see Fig. 9c).

The DRV structure of the TMAZ maintained a microhardness level almost similar to that of the SZ due to the presence of high dislocation density. As mentioned above, higher rotational speeds facilitated the extension of the refined grain structure into the second plate due to more intense material softening. Consequently, sample S-1 exhibited the most homogeneous microhardness distribution with a slight overall decrease (Fig. 11c), while sample S-2 showed a decrease of microhardness within the SZ-TMAZ transition area of mixed nature.

3.5 Mechanical testing

Figure 12a represents the histogram of the maximum force values obtained from the tensile lap shear tests. Samples made at 2000 rpm revealed the highest mechanical strength with the most stable behavior throughout all repetitions. The average strength value of 13.6 ± 0.5 kN was reached through favorable plug fracture by tearing around the spot weld periphery (Fig. 12c). Notably, this result exceeds the data reported in other studies on P-FSSW with featured shoulders [e.g., 22, 29, 36]. This improvement was attributed to a homogeneous microstructure within the joining interface, where a gradual microstructural evolution reduced stresses [14]. In contrast, the spot welds made at 2500 rpm experienced a decrease in average mechanical strength to 9.9 ± 3.0 kN. Moreover, the results have shown significantly lower repeatability. Such remarkable variation was attributed to the formation of the centerline hook, which acted as a high-stress nucleation and, thereby, differently affected the final fracture manner (see Fig. 4c and Fig. 12d–e).

Two types of fracture mode were fixed among the series of spot welds samples made with 2500 rpm such as

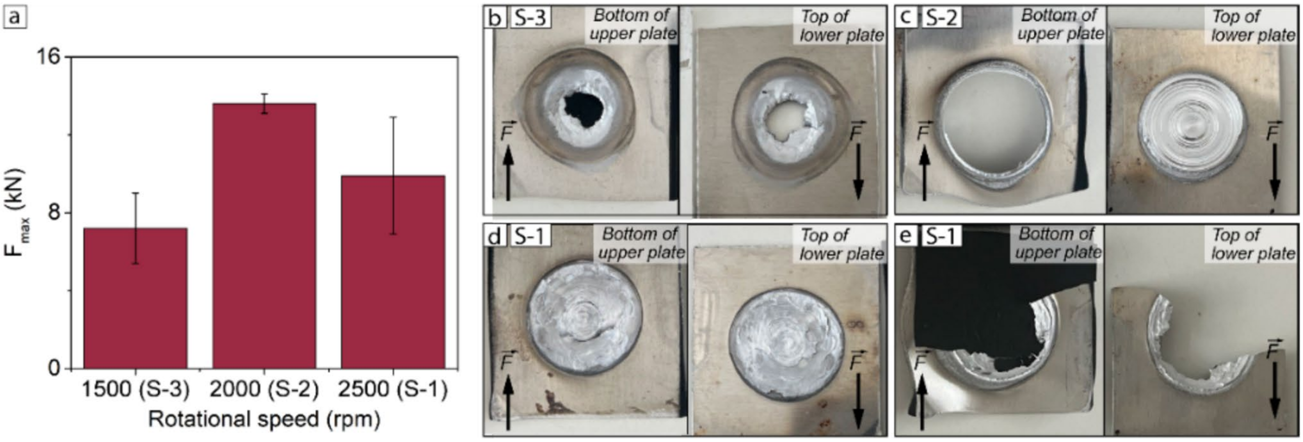

Fig. 12 (**a**) Mechanical resistance of spot welds versus applied rotational speed in different samples. Fracture of samples (**b**) S-3, (**c**) S-2, and (**d–e**) S-1

an interfacial fracture (Fig. 12d) and complete distortion (Fig. 12e). Conversely, the spot welds made at a rotational speed of 1500 rpm showed the lowest mechanical strength (7.2 ± 1.8 kN) due to limited plastic deformation along the joining interface. Thus, the interfacial fracture beneath the shoulder edge in this sample did not experience bonding between the plates but rather only a plastic deformation (Fig. 12b).

To confirm the discussed results presented in Fig. 12a, a one-way ANOVA was conducted to assess the impact of rotation speed on the $F_{\max}$ values of welds. In this analysis, the variability of $F_{\max}$ values is partitioned into two components: the variability between the groups (different rotation speeds) and the variability within the groups. The F statistic, calculated by dividing the mean squares of the groups by the mean squares of the error, resulted in a value of 10.07. This high F statistic value indicates that the group variability (attributable to different rotation speeds) is significantly greater than within the groups. The p value associated with the F statistic is 0.0121, less than the significance level of 0.05. This indicates that the differences among the groups are statistically significant at a 95% confidence level. Therefore, it can be concluded that rotation speed significantly affects the $F_{\max}$ values, which are strongly correlated with the extent of material plasticization and its flow. If the p value had been greater than 0.05, it would not have been possible to reject the null hypothesis, suggesting that the differences between the rotation speeds are not statistically significant.

4 Conclusions

The present study examined the effect of rotational speed on microstructure development and mechanical properties of dissimilar aluminum plates joined by P-FSSW. The main results demonstrate the promising results of producing strength solid-state welds using a flat featureless tool. The following key findings can be drawn:

- The joining materials have experienced axisymmetric plastic deformation beneath the whole shoulder diameter. The absence of the shoulder features mitigated centerline downward material flow, thereby eliminating common defect of the edge hook.
- An increase in rotational speed facilitated material softening from the surface toward the bulk of the spot welds, where microstructure development evolved through a gradual transition, shifting from the mechanism of CDRX (within the SZ) to DRV (within the TMAZ). The development of DRV proved highly sensitive to rotational speed within the 2000–2500 rpm range. The application the highest rotational speed expanded TMAZ region, forming a centerline hook.
- Microhardness distribution displayed stable uniform distribution across the thermo-mechanically treated microstructure resulted from a balanced interplay between re-precipitated strengthening Al2CuMg phases and grain refinement. These findings demonstrate the promising potential of flat featureless shoulders as a surface mechanical treatment tool.
- Mechanical response demonstrated a linear relation with the intensity of material softening and its flow along the joining interface. Spot welds produced within the 1500–2000 rpm rotational speed range demonstrated stable behavior of a maximum 13.6 ± 0.5 kN. In contrast, the formation of a centerline hook at 2500 rpm of rotational speed significantly reduced the maximum force to 9.9 ± 3.0 kN, thereby limiting optimal process window within the 1500–2000 rpm range.

Acknowledgements This work was partly supported by the «World-Class Science Center State Marine Technical University, 190121 St. Petersburg, Russia» program Advanced Digital Technologies (Grant Agreement No. 075-15-2022-312, dated 20 April 2022).

Author contribution Conceptualization, N.C. and D.P.; data curation, M.R. and G.D.; formal analysis M.R. and G.D; methodology, N.C. and D.P.; supervision, G.C. and U.G.; validation, N.C. and D.P.; writing—original draft, M.R. and G.D; writing—review and editing, N.C., D.P., U.G. and G.C. All authors have read and agreed to the published version of the manuscript.

Funding Open access funding provided by Politecnico di Bari within the CRUI-CARE Agreement.

Data availability The data that support the findings of this study are available from the corresponding author upon request.

Declarations

Competing interests The authors declare no competing interests.

References

1. Stavropoulos P, Sabatakakis K (2024) Quality assurance in resistance spot welding: state of practice, state of the art, and prospects. Metals 14(2):185. https://doi.org/10.3390/met14020185
2. Padhy GK, Wu CS, Gao S (2018) Friction stir based welding and processing technologies-processes, parameters, microstructures and applications: a review. JMST 34:1–38. https://doi.org/10.1016/j.jmst.2017.11.029
3. Shen Z, Ding Y, Gerlich AP (2020) Advances in friction stir spot welding. Crit Rev Solid State Mater Sci 45:457–534. https://doi.org/10.1080/10408436.2019.1671799
4. M. Media Release, Mazda develops world's first aluminum joining technology using friction heat, Feb. 27, 2003. https://newsroom.mazda.com/en/publicity/release/2003/200302/0227e.html. Accessed 12 Jan 2025
5. Badarinarayan H, Hunt F, Okamoto K (2007) Friction stir spot welding. In: Mishra RS, Mahoney MW (eds) Friction Stir Welding and Processing. ASM, Materials Park, OH, p 235
6. Prabhakar DAP, Shettigar AK, Herbert MA, Patel M, Pimenov DY, Giasin K, Prakash C (2022) A comprehensive review of friction stir techniques in structural materials and alloys: challenges and trends. JMR&T 20:3025–3060. https://doi.org/10.1016/j.jmrt.2022.08.034
7. Guishen Y, Xin C, Zitao W (2022) Mechanical performance optimization and microstructure analysis of similar thin AA6061-T6 sheets produced by swept friction stir spot welding. J Adv Manuf Technol 118:1829–1841. https://doi.org/10.1007/s00170-021-07387-7
8. Chen K, Liu X, Ni J (2017) Keyhole refilled friction stir spot welding of aluminum alloy to advanced high strength steel. J Mater Process Technol 249:452–462. https://doi.org/10.1016/j.jmatprotec.2017.06.039
9. Ke WC, Oliveira JP, Ao SS, Teshome FB, Chen L, Peng B, Zeng Z (2022) Thermal process and material flow during dissimilar double-sided friction stir spot welding of AZ31/ZK60 magnesium alloys. JMR&T 17:1942–1954. https://doi.org/10.1016/j.jmrt.2022.01.097
10. Sun Y, Fujii H, Zhu S, Guan S (2019) Flat friction stir spot welding of three 6061–T6 aluminum sheets. J Mater Process Technol 264:414–421. https://doi.org/10.1016/j.jmatprotec.2018.09.031
11. Han J, Paidar M, Vignesh RV, Mehta KP, Heidarzadeh A, Ojo OO (2020) Effect of shoulder features during friction spot extrusion welding of 2024–T3 to 6061–T6 aluminium alloys. Arch Civil Mech Eng 20:1–17. https://doi.org/10.1007/s43452-020-00086-2
12. Zou Y, Li W, Shen Z, Su Y, Yang X (2023) Refill friction stir spot welding of aluminum alloys: state-of-the-art and perspectives, Weld. World 67:1853–1885. https://doi.org/10.1007/s40194-023-01552-0
13. Silva BH, Zepon G, Bolfarini C, dos Santos JF (2020) Refill friction stir spot welding of AA6082-T6 alloy: hook defect formation and its influence on the mechanical properties and fracture behavior. Mater Sci Eng A 773:138724. https://doi.org/10.1016/j.msea.2019.138724
14. Becker N, dos Santos JF, Klusemann B (2024) Experimental investigation of crack propagation mechanism in refill friction stir spot joints of AA6082-T6. Eng Fract Mech 300:109963. https://doi.org/10.1016/j.engfracmech.2024.109963
15. Tra TH, Okazaki M, Suzuki K (2012) Fatigue crack propagation behavior in friction stir welding of AA6063-T5: Roles of residual stress and microstructure. Int J Fatigue 43:23–29. https://doi.org/10.1016/j.ijfatigue.2012.02.003
16. Rostamiyan Y, Seidanloo A, Sohrabpoor H, Teimouri R (2015) Experimental studies on ultrasonically assisted friction stir spot welding of AA6061. Arch Civ Mech Eng 15:335–346. https://doi.org/10.1016/j.acme.2014.06.005
17 Bagheri B, MahdianRizi AA, Abbasi M, Givi M (2019) Friction stir spot vibration welding: improving the microstructure and mechanical properties of Al5083 joint. MMA 8:713–725. https://doi.org/10.1007/s13632-019-00563-y
18. Campanelli SL, Casalino G, Casavola C, Moramarco V (2013) Analysis and comparison of friction stir welding and laser assisted friction stir welding of aluminum alloy. Mate 6:5923–5941. https://doi.org/10.3390/ma6125923
19. Bakavos D, Chen Y, Babout L, Prangnell P (2011) Material interactions in a novel pinless tool approach to friction stir spot welding thin aluminum sheet. MMTA 42:1266–1282. https://doi.org/10.1007/s11661-010-0514-x
20. Tozaki Y, Uematsu Y, Tokaji K (2010) A newly developed tool without probe for friction stir spot welding and its performance. J Mater Process Technol 210:844–851. https://doi.org/10.1016/j.jmatprotec.2010.01.015
21. Li W, Li J, Zhang Z, Gao D, Wang W, Dong C (2014) Improving mechanical properties of pinless friction stir spot welded joints by eliminating hook defect. Mater Des 62:247–254. https://doi.org/10.1016/j.matdes.2014.05.028
22. Chu X, Yin M, Gao J, Wang X, Wang Y (2020) Effects of shoulder geometry on microstructures and mechanical properties of probeless friction stir spot welded aluminum 7075–T651 sheets. Metals 10(12):1605. https://doi.org/10.3390/met10121605
23. Yang X, Feng W, Li W, Xu Y, Chu Q, Ma T, Wang W (2018) Numerical modeling and experimental investigation of thermal and material flow in probeless friction stir spot welding process of Al 2198–T8. SCI TECHNOL WELD JOI 23:704–714. https://doi.org/10.1080/13621718.2018.1469832
24. Cox CD, Gibson BT, Strauss AM, Cook GE (2014) Energy input during friction stir spot welding. J Manuf Process 16:479–484. https://doi.org/10.1016/j.jmapro.2014.05.007
25. Zhang L, Ji S, Luan G, Dong C, Fu L (2011) Friction stir welding of Al alloy thin plate by rotational tool without pin. JMST 27:647–652. https://doi.org/10.1016/S1005-0302(11)60120-5
26. Li W, Li J, Zhang Z, Gao D, Wang W, Luan G (2014) Pinless friction stir welding of AA2024-T3 joint and its failure modes. Trans Tianjin Univ 20:439–443. https://doi.org/10.1007/s12209-014-2157-2
27. Contuzzi N, Rashkovets M, Casalino G (2023) Numerical and experimental investigation of probeless friction stir spot welding of a multilayer aluminum alloy compound. Sci Technol Weld Join 28:653–661. https://doi.org/10.1080/13621718.2023.2193460
28. Chu Q, Hao SJ, Li WY, Yang XW, Zou YF, Wu D (2021) Impact of shoulder morphology on macrostructural forming and the texture development during probeless friction stir spot welding. JMR&T 12:2042–2054. https://doi.org/10.1016/j.jmrt.2021.04.013
29. Chu Q, Li WY, Yang XW, Shen JJ, Li YB, Wang WB (2017) Study of process/structure/property relationships in probeless friction stir spot welded AA2198 Al-Li alloy. Weld World 61:291–298. https://doi.org/10.1007/s40194-017-0423-3
30. Aota K, Ikeuchi K (2009) Development of friction stir spot welding using rotating tool without probe and its application to low-carbon steel plates. Weld 23:572–580. https://doi.org/10.1080/09507110802543054
31. Rashkovets M, Contuzzi N, Casalino G (2022) Modeling of probeless friction stir spot welding of AA2024/AISI304 steel lap joint. Mater 15:8205. https://doi.org/10.3390/ma15228205
32. Alaeibehmand S, Ranjbarnodeh E, Mirsalehi SE (2021) Joining mechanism in pinless FSSW of aluminum-steel with or without Zn and brass interlayers. Mater Charact 180:111400. https://doi.org/10.1016/j.matchar.2021.111400

33. Rashkovets M, Palmieri ME, Contuzzi N, Tricarico L, Casalino G (2024) Dissimilar probeless friction stir spot welding of aluminum alloy and USIBOR® 1500-AS steel thin plates. J Manuf Mater 8:55. https://doi.org/10.3390/jmmp8020055
34. Kuang B, Shen Y, Chen W, Yao X, Xu H, Gao J, Zhang J (2015) The dissimilar friction stir lap welding of 1A99 Al to pure Cu using Zn as filler metal with "pinless" tool configuration. Mater Des 68:54–62. https://doi.org/10.1016/j.matdes.2014.12.008
35. Shin HS, de Leon M (2016) Weldability assessment of friction stir spot welded lightweight alloys using pin and pinless tools. Sci Technol Weld Join 21(2):99–105. https://doi.org/10.1179/1362171815Y.0000000070
36. Y. Guishen, C. Xin, W. Zitao, Z. Guanchen, C. Yixiong (2024) Microstructure and mechanical performances analyses on probeless friction stir spot welds of AA6061-T6 aluminum sheets, https://www.researchsquare.com/article/rs-1014036/v1, May 23, 2024
37. Chiou YC, Liu CT, Lee RT (2013) A pinless embedded tool used in FSSW and FSW of aluminum alloy. J Mater Process Technol 213:1818–1824. https://doi.org/10.1016/j.jmatprotec.2013.04.018
38. Chu Q, Yang XW, Li WY, Li YB (2016) Microstructure and mechanical behaviour of pinless friction stir spot welded AA2198 joints. Sci Technol Weld Join 21:164–170. https://doi.org/10.1179/1362171815Y.0000000078
39. Huang KE, Logé RE (2016) A review of dynamic recrystallization phenomena in metallic materials. Mater Des 111:548–574. https://doi.org/10.1016/j.matdes.2016.09.012
40. Butola R, Pandit D, Pratap C, Chandra P (2022) Two decades of friction stir processing–a review of advancements in composite fabrication. JAST 36:795–832. https://doi.org/10.1080/01694243.2021.1938835
41. Keerthipalli T, Aepuru R, Biswas A (2023) Review on precipitation, intermetallic and strengthening of aluminum alloys. Proc Inst Mech Eng, Part B 237(6–7):833–850. https://doi.org/10.1177/09544054221111901
42. Ma Z, Feng A, Chen D, Shen J (2018) Recent advances in friction stir welding/processing of aluminum alloys: microstructural evolution and mechanical properties. CRIT REV SOLID STATE 43(4):269–333. https://doi.org/10.1080/10408436.2017.1358145
43. Aluminum 2024-T4; 2024-T351. https://asm.matweb.com/search/specificmaterial.asp?bassnum=ma2024t4
44. Aluminum 6082-T6. https://www.matweb.com/search/datasheet_print.aspx?matguid=fad29be6e64d4e95a241690f1f6e1eb7
45. B. Robitaille, P. l R. Provencher, L. St-Georges, M. Brochu, (2021) Mechanical properties of 2024-T3 AlClad aluminum FSW lap joints and impact of surface preparation. Int J Fatigue 143 105979 https://doi.org/10.1016/j.ijfatigue.2020.105979
46. G. Dell'Avvocato, M. Rashkovets, A. Castellano, D. Palumbo, N. Contuzzi, G. Casalino, U. Galietti, Preliminary procedure for the assessment of probeless friction stir spot welds (P-FSSW) in dissimilar aluminum alloys by long pulsed laser thermography, SPIE Proceedings 13047 (2024), Thermosense: Thermal Infrared Applications XLVI; 130470R. https://doi.org/10.1117/12.3013618
47. Reilly A, Shercliff H, Chen Y, Prangnell P (2015) Modelling and visualisation of material flow in friction stir spot welding. J Mater Process Technol 225:473–484. https://doi.org/10.1016/j.jmatprotec.2015.06.021
48. Chen H, Fu L, Liang P, Liu F (2017) Defect features, texture and mechanical properties of friction stir welded lap joints of 2A97 Al-Li alloy thin sheets. Mater Charact 125:160–173. https://doi.org/10.1016/j.matchar.2017.01.038
49. Yang Q, Mironov S, Sato YS, Okamoto K (2010) Material flow during friction stir spot welding. Mater Sci Eng A 527:4389–4398. https://doi.org/10.1016/j.msea.2010.03.082
50. Kayser T (2011) Characterization of microstructure in aluminum alloys based on electron backscatter diffraction, Ph.D. Thesis Technical University of Dortmund. Dortmund, Germany. https://core.ac.uk/download/pdf/46911367.pdf. Accessed 12 Jan 2025
51. Kolubaev AV, Zaikina AA, Sizova OV, Ivanov KV, Filippov AV, Kolubaev EA (2018) On the similarity of deformation mechanisms during friction stir welding and sliding friction of the AA5056 alloy. Russ Phys J 60:2123–2129. https://doi.org/10.1007/s11182-018-1335-4
52. Chen X, Han Z, Lu K (2015) Enhancing wear resistance of Cu–Al alloy by controlling subsurface dynamic recrystallization. Scr Mater 101:76–79. https://doi.org/10.1016/j.scriptamat.2015.01.023
53. Jacquin D, Guillemot G (2021) A review of microstructural changes occurring during FSW in aluminium alloys and their modelling. J Mater Process Technol 288:116706. https://doi.org/10.1016/j.jmatprotec.2020.116706
54. Z. W. Chen, T. Pasang, Y. Qi, Mater (2008) Shear flow and formation of Nugget zone during friction stir welding of aluminium alloy 5083-O, Sci Eng A 474.1–2 312–316 https://doi.org/10.1016/j.msea.2007.05.074
55. Xie J, Zhu Y, Bian F, Liu C (2017) Dynamic recovery and recrystallization mechanisms during ultrasonic spot welding of Al-Cu-Mg alloy. Mater Charact 132:145–155. https://doi.org/10.1016/j.jmatprotec.2020.116706
56. Hughes DA, Hansen N (1997) High angle boundaries formed by grain subdivision mechanisms. Acta Mater 45:3871–3886
57. Mironov S, Inagaki K, Sato YS, Kokawa H (2015) Effect of welding temperature on microstructure of friction-stir welded aluminum alloy 1050. METALL MATER TRANS A 46:783–790. https://doi.org/10.1007/s11661-014-2651-0
58. Upadhyay P, Reynolds AP (2012) Effects of forge axis force and backing plate thermal diffusivity on FSW of AA6056. Mater Sci Eng A 558:394–402. https://doi.org/10.1016/j.msea.2012.08.018
59. Mironov S, Sato YS, Kokawa H (2009) Development of grain structure during friction stir welding of pure titanium. Acta Mater 57(15):4519–4528. https://doi.org/10.1016/j.actamat.2009.06.020
60. Shen J, Lage SBM, Suhuddin UFH, Bolfarini C, Dos Santos JF (2018) Texture development and material flow behavior during refill friction stir spot welding of AlMgSc. MMTA 49:241–254. https://doi.org/10.1007/s11661-017-4381-6
61. Fonda RW, Knipling KE (2011) Texture development in friction stir welds. Sci Technol Weld Join 16:288–294. https://doi.org/10.1179/1362171811Y.0000000010
62. Cai B, Zheng ZQ, He DQ, Li SC, Li HP (2015) Friction stir weld of 2060 Al–Cu–Li alloy: microstructure and mechanical properties. J Alloys Compd 649:19–27. https://doi.org/10.1016/j.jallcom.2015.02.124
63. Mousavi SH, Anijdan D, Sadeghi-Nezhad H, Lee W, Shin N, Park MJ, Nayyeri HR, Jafarian ARE, TEM, (2021) study of S'hardening precipitates in the cold rolled and aged AA2024 aluminum alloy: influence on the microstructural evolution, tensile properties & electrical conductivity. JMR&T 13:798–807. https://doi.org/10.1016/j.jmrt.2021.05.003
64. Genevois C, Deschamps A, Denquin A, Doisneau-Cottignies B (2005) Quantitative investigation of precipitation and mechanical behaviour for AA2024 friction stir welds. Acta Mater 53(8):2447–2458. https://doi.org/10.1016/j.actamat.2005.02.007